Imaging Strategies for Hyperpolarized Elements and Molecules

John P. Mugler, III, Ph.D.

Center for In-vivo Hyperpolarized Gas MR Imaging, Department of Radiology
University of Virginia School of Medicine
Charlottesville, VA, USA

Background

Nuclear magnetic resonance is an extremely valuable and versatile tool, finding a wide variety of applications in numerous fields of study. Nonetheless, under typical experimental conditions, the nuclear polarization, P, where:

$$P = \frac{|N_+ - N_-|}{N_+ + N_-}, \qquad [1]$$

and N_+ and N_- are the spin populations in the lower and upper energy states, respectively, is at most on the order of 10^{-4}. Because of this low polarization at thermal equilibrium, there has been a constant drive for higher field systems, improved RF coil designs, and low-noise receiver systems to raise the signal-to-noise ratio (SNR) and thereby permit increased spatial, temporal or spectral resolution. Considering this aspect of the NMR phenomenon, the prospect of being able to increase the polarization level by any substantial amount would suggest the possibility for a significant improvement of the affected applications. Such a prospect has recently been realized with the development of *hyperpolarized* substances for MR imaging and spectroscopy, wherein nuclear polarizations approaching 100% are possible.

Biological MR studies with hyperpolarized substances have been focused on three spin-½ nuclei, including the non-radioactive noble-gas isotopes ^{3}He [1-4] and ^{129}Xe [5-8], and the carbon isotope ^{13}C as a component of several organic molecules [9-12]. The magnetogyric ratios and natural abundance for these three nuclei, and the diffusion coefficients and solubility for the two noble gases, are listed in Table I. Methods used for hyperpolarization include optical pumping and spin exchange (^{3}He, ^{129}Xe) [16,17], metastability exchange (^{3}He) [18,19], parahydrogen-induced polarization (^{13}C) [20,21] and dynamic nuclear polarization (^{13}C) [22,23]. Polarizations of approximately 50% can be achieved routinely for liter quantities of the noble gases, while the recently reported polarizations for ^{13}C compounds are about half as much. A discussion of polarization methods can be found in the syllabus contribution by Bastiaan Driehuys for this course, *Alternate Mechanisms for Spin Polarization*.

Although the natural abundance of ^{3}He is negligible, it is produced from the nuclear decay of tritium and currently can be purchased for approximately 100 USD per liter (STP). Natural-abundance xenon (26% ^{129}Xe) is relatively inexpensive (ca. 10 USD per liter), while isotopically enriched xenon is relatively expensive (ca. 250 USD per liter for 70-80% ^{129}Xe). The cost for ^{13}C depends on the molecule; for example, 1 gram of ^{13}C (99%) urea costs ca. 85 USD.

Both ^{3}He and ^{129}Xe are useful for imaging of gas-filled spaces, such as cracks and voids in materials [24], or the lung, colon and sinuses in humans and animals [1-6,8,25,26]. For direct visualization of gas-space morphology, ^{3}He has the advantage that the magnetogyric ratio (and hence magnetic moment) is 2.8 times larger than that for ^{129}Xe. Assuming the thermal noise in the NMR experiment is dominated by losses in the sample or subject, it is straightforward to show that the SNR for hyperpolarized substances is directly proportional to the magnetogyric ratio, and does not vary with frequency as in the thermal-equilibrium case [1,2,27]. Thus, for equivalent experimental conditions, ^{3}He would appear to have a substantial (3-fold) SNR advantage over ^{129}Xe. Depending on the experimental conditions, however, the 30-fold lower diffusion constant [14] and lower magnetogyric ratio of ^{129}Xe may act in its favor. For example, the lower diffusion constant would yield less signal attenuation for high-resolution imaging, and the lower magnetogyric ratio would result in decreased dephasing due to off-resonance effects, such as from magnetic-susceptibility interfaces. On the other hand, the high diffusion constant of ^{3}He may prove ideal for characterizing the microstructure of complex gas spaces such as the lung [28-30].

Table I. Properties of ^{3}He, ^{129}Xe and ^{13}C.

Nucleus	Magnetogyric Ratio [MHz/T]	Natural Abundance [%]	Self-Diffusion Coefficient[1]	Ostwald Solubility Coefficient[2]		
				Water	Blood	Oil
^{3}He	-32.4	10^{-4}	1.8	0.0098	0.0099	0.018
^{129}Xe	-11.8	26	0.06	0.083	0.14	1.7
^{13}C	10.7	1	--	--	--	--

1. Data are in cm^2/s at 1 atm. and 20°C. Helium data from ref. 13; xenon data from ref. 14.
2. Volume of gas at 1 atm. that dissolves in unit volume of fluid. Data are for 37°C and natural abundance gases [15].

As indicated in Table I, ^{129}Xe gas is soluble in a variety of substances, while ^{3}He gas in general has a very low solubility [15]. In particular, xenon is lipophilic, having a high solubility in oils and lipid-containing tissues. Another important characteristic of ^{129}Xe is an exquisite sensitivity to its environment that results in an enormous range of chemical shifts upon solution (e.g., a range of approximately 200 ppm in common solvents) or adsorption [31]. These solubility and chemical shift characteristics make ^{129}Xe a valuable probe for a variety of material science and biological applications. However, for human applications, xenon presents the complication of being a general anesthetic in high concentrations (> 70%).

Although both ^{3}He and ^{129}Xe can be prepared in injectable forms (e.g., biologically-compatible solvent carriers for ^{129}Xe [32,33] and microbubbles for ^{3}He [34]) for medical applications such as angiography or organ perfusion, ^{13}C has the important advantage that its molar concentration in solutions of carbon-based molecules can be at least an order of magnitude greater than the concentrations of either ^{3}He or ^{129}Xe in injectable preparations. Thus, hyperpolarized ^{13}C-based compounds provide a superior combination of SNR, spatial resolution and temporal resolution for this class of applications [9-12,35]. In addition, since carbon-based molecules play a critical role in the functioning of living organisms, the use of appropriate molecules containing hyperpolarized ^{13}C presents the opportunity to rapidly and non-invasively assess various metabolic processes [10].

Imaging Strategies

For typical MR imaging conditions, certain characteristics of hyperpolarized nuclei differ substantially from those for water or lipid protons in biological tissues. Hence, these differences play an important role in the selection and optimization of appropriate pulse sequences for imaging of hyperpolarized substances. Compared to water or lipid protons in biological tissue, important characteristics of hyperpolarized nuclei include:

1. Longitudinal magnetization is not at thermal equilibrium in the static magnetic field of the scanner;
2. Relaxation times are typically much longer;
3. Diffusivity is much higher (^{3}He and ^{129}Xe gases);
4. States that have substantially different chemical shifts are in dynamic exchange (^{129}Xe in the lung or in other porous materials); and
5. Longitudinal relaxation rate is directly proportional to the concentration of oxygen (^{3}He and ^{129}Xe gases in the lung).

The first three characteristics have a general impact on the design of pulse sequences for imaging of hyperpolarized substances, and so the effect of these characteristics on sequence selection and optimization will be discussed in detail below. The fourth characteristic leads to interesting possibilities for deriving functional information about the lung by using ^{129}Xe imaging or spectroscopy. For information on this topic, the reader is referred to references 36-40. The fifth characteristic makes it possible to measure the partial pressure of oxygen and the rate of oxygen consumption in the lung by using ^{3}He imaging. The reader is referred to references 41-44 for information on this topic.

Non-equilibrium Magnetization and Long Relaxation Times

First, we will consider substances for which only characteristics 1 and 2 apply: hyperpolarized ^{13}C compounds and injectable forms of hyperpolarized ^{3}He or ^{129}Xe. The T1 relaxation times for these substances are typically tens of seconds [9-12,32-35,45]. There is relatively little data on the T2 relaxation times, although in many cases (excluding those that involve rapid exchange of ^{129}Xe between sites) it is reasonable to expect that the T2 will be a significant fraction of the T1. These long relaxation times favor the use of a single-shot, echo-train acquisition so that all (or at least a significant fraction) of the slowly decaying non-equilibrium magnetization can be sampled repeatedly before it decays back to thermal equilibrium. A fully "balanced" (i.e., zeroth gradient moments along each axis equal to zero over a TR period) gradient-echo (GRE) pulse sequence such as TrueFISP [46] is well suited for this purpose [10-12,35]. In recent years, such fully-balanced pulse sequences have been widely used for cardiovascular applications. But, due to the long relaxation times of hyperpolarized substances, the appropriate parameter values for hyperpolarized imaging are different than those for proton imaging. As illustrated in Figure 1b, when the T1 and T2 relaxation times are longer than the acquisition time (e.g., the solid and dotted curves in the center and right plots of Fig. 1b), which is often the case for hyperpolarized applications, the maximum signal is obtained for flip angles of approximately 180º [10,35]. In contrast, for proton relaxation times of interest in biological tissue (e.g., the dashed curve in the left plot of Fig. 1a), maximum signal is obtained for flip angles less than 90º. (Figure 1 shows the predicted on-resonance signal behavior for an ideal TrueFISP-type pulse sequence. The technical details of this class of pulse sequences, including the off-resonance signal behavior, are discussed in the syllabus contribution by Brian Hargreaves for this course, *Fast Gradient Echo Including SSFP*.)

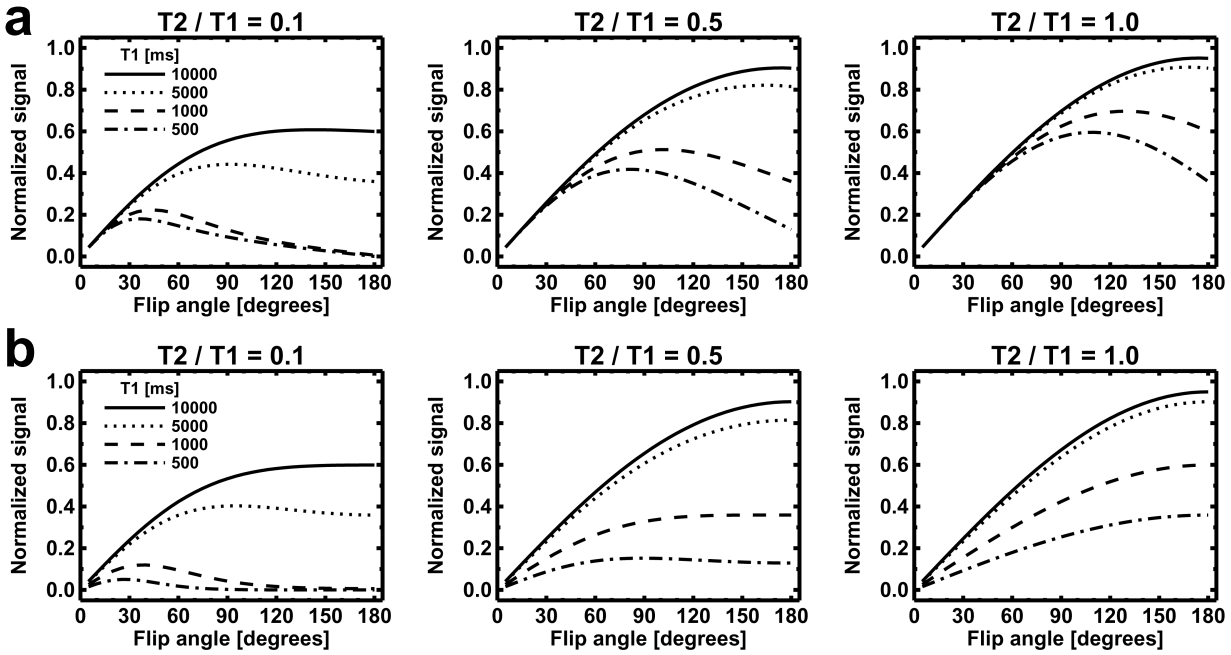

Figure 1. On-resonance signal behavior for an ideal TrueFISP-type pulse sequence with a total acquisition time of 1 second (TR 4 ms, sequential phase encoding, 256 phase-encoding steps, half-angle preparation pulse [49]). For (**a**) thermal magnetization and (**b**) hyperpolarized magnetization, the variation of the normalized signal with flip angle is shown for a range of T1 and T2 relaxation times. The normalized signal was calculated as that associated with the central phase-encoding step. Slice-profile and diffusion effects were not included in the calculations.

Since the hyperpolarized magnetization is typically several orders of magnitude larger than the corresponding thermal-equilibrium value, T1 relaxation of the hyperpolarized magnetization essentially amounts to a decay of the magnetization toward zero. Figure 1 shows signal versus flip-angle curves for both thermal (Fig. 1a) and hyperpolarized (Fig. 1b) magnetization. For relaxation times that are long compared to the acquisition time (e.g., the solid and dotted curves), differences between the results for thermal and hyperpolarized magnetization are small. However, for shorter relaxation times (e.g., the dashed and dash-dot curves), both the flip angles that result in the

maximum signal and the signal intensities for thermal magnetization differ from those for hyperpolarized magnetization. For a much longer acquisition time than that considered in Figure 1 (e.g., for a 3D acquisition), the non-equilibrium nature of the hyperpolarized magnetization would also have a significant influence on the signal behavior for the 5000 and 10000-ms T1 relaxation times. Also note that techniques that require multiple excitations with high-flip-angle RF pulses (e.g., conventional spin-echo imaging) are not suitable for the non-equilibrium magnetization of hyperpolarized substances unless fresh hyperpolarized material can be supplied to the volume of interest throughout the imaging experiment.

Although the T2 times for hyperpolarized substances are often long compared to those for biological tissues, they are nonetheless shorter than the corresponding T1 times. Thus, if a series of images at discrete time points is desired, it is useful to use a DEFT-type configuration [47] so that between image acquisitions the remaining hyperpolarized magnetization is stored along the longitudinal axis [10,35,48]. In TrueFISP acquisitions, this is often referred to as using a "flip-back" [48] or "restore" RF pulse.

Given the long T2 relaxation times involved, a single-shot fast/turbo spin-echo pulse sequence (FSE/TSE) can also be effective for this imaging application [9], and a flip-back RF pulse can also be used with this pulse sequence. However, due to its fully-balanced gradient structure, the TrueFISP pulse sequence is in general more resistant to signal loss or ghost artifacts from motion, and thus would likely be preferred over FSE/TSE as long as adequate static-field homogeneity can be achieved for the application at hand.

High Diffusivity

In addition to non-equilibrium magnetization and long relaxation times, ^{3}He and ^{129}Xe gases also possess the third characteristic listed above – high diffusivity. The self-diffusion coefficients for these gases (Table 1) are several orders of magnitude larger than that for water in biological tissues, and as a result even the magnetic-field gradients used for spatial encoding can cause substantial signal attenuation. There are both positive and negative aspects to this circumstance. On the positive side, we can take advantage of diffusion-induced signal attenuation to measure the apparent diffusion coefficient (ADC) of the gases in structures such as the lung. For example, it has been shown that the ADC varies depending on the status of the lung microstructure [28-30,50]. While this is an important application for hyperpolarized gases, here we will concentrate on negative aspects of diffusion-induced signal attenuation secondary to the high diffusivity – limited spatial resolution in echo-train pulse sequences and reduced SNR.

Assuming isotropic, unrestricted diffusion (i.e., measured diffusion coefficients independent of the timing, strength and direction of diffusion-sensitization gradients), it is straightforward to calculate the signal attenuations that correspond to various pulse-sequence types and parameter-value settings. However, one of the primary applications for hyperpolarized gases is imaging of the lung, which is a complex, restricted diffusion environment. For this application, it has been shown that the ADC depends on the timing, strength and direction of diffusion-sensitization gradients [50-55]. Nonetheless, by using the mathematical formalism appropriate for isotropic, unrestricted diffusion, by restricting our attention to a specific time scale (typically a few milliseconds), and by choosing ADC values that are representative of the chosen time scale and the condition of the lung tissue, we can calculate signal-attenuation values which approximate those obtained in the lung and thus provide useful guidance for the design of pulse sequences for imaging the lung. Even so, the reader should keep in mind the limitations of this approach when applying the results discussed below to any particular application of interest.

To understand how gradient-waveform design affects the resulting diffusion-induced signal attenuation, it is useful to recall that the *b* value associated with a gradient waveform can be calculated as the integral of the squared magnitude of the *k*-space trajectory [56]. This relationship is extremely useful as an intuitive guide for the design of pulse sequences; a simplified example is useful to illustrate the concept. Consider the standard (monopolar) readout gradient waveform typically used in a RARE-type [57] spin-echo-train pulse sequence compared to the fully-balanced readout gradient waveform used in TrueFISP – which of these yields lower diffusion-induced signal attenuation? Figure 2 shows these two gradient waveforms (from the center of a given echo to the center of the next echo) along with the corresponding $|k|^2$ curves. Even though the gradient is active for twice as long for the TrueFISP case, the *b* value (which is the area under the $|k|^2$ curve) corresponding to one echo spacing for the fully-balanced readout gradient is only one-third of that for the monopolar readout gradient. For the RARE case, the *k*-space trajectory remains at a high spatial frequency between readout events, whereas for the TrueFISP case the trajectory returns to the center of *k* space between readout events, resulting in a much lower *b* value for the TrueFISP case and hence a correspondingly lower signal attenuation.

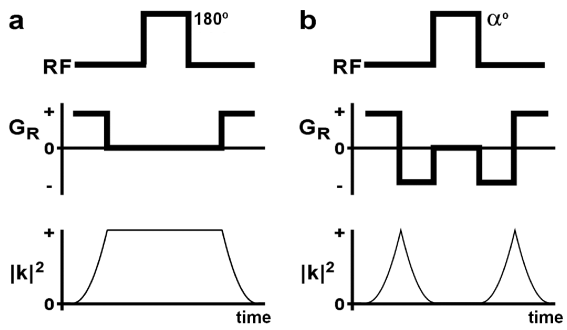

Figure 2. Analysis of the diffusion sensitivity from a given echo time to the next for the readout gradient waveforms in simplified (**a**) RARE and (**b**) TrueFISP pulse sequences. The RF and readout-gradient (G_R) timing, and the associated waveforms for the squared-magnitude of the *k*-space trajectory ($|k|^2$) are shown for each sequence. The *b* value is the area under the $|k|^2$ curve.

Figure 3 shows calculated signals versus echo number for monopolar (RARE) and balanced (TrueFISP) readout gradients and three nominal spatial resolutions, assuming that the echo trains are generated by using 180º RF pulses. We see that diffusion-induced signal attenuation for the balanced readout gradient is substantially less than that for the monopolar readout gradient, consistent with the analysis above. Diffusion-induced signal attenuation during the echo train ultimately limits the spatial resolution by widening the point spread function and also decreases the SNR for the central portion of *k* space unless centric phase encoding is used.

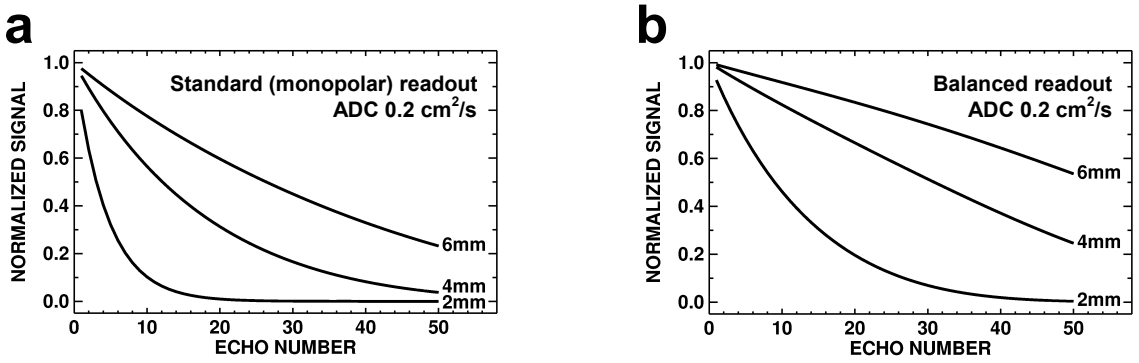

Figure 3. Theoretical calculations of normalized signal versus echo number for echo-train pulse sequences that use (**a**) standard (monopolar) and (**b**) balanced readout gradients. For both cases, 180º RF pulses were used to generate the echo train. The plots illustrate the diffusion-induced signal attenuations for nominal spatial resolutions of 2, 4, and 6 mm that result from an ADC of 0.2 cm^2/s, which corresponds to ^{3}He in a healthy human lung. The calculations included the signal-attenuation effects of a centrically-ordered phase-encoding gradient.

Results from previous studies support these theoretically-predicted differences between the diffusion sensitivities of RARE and TrueFISP pulse sequences. In a recent study of ^{3}He lung imaging by Durand et al. [58], a minimum resolution of 6 mm was postulated for a RARE-type pulse sequence based on an attenuation limit of 37% for the signal remaining at the end of a 36-echo train. In contrast, in preliminary evaluations of a TrueFISP-type pulse sequence for ^{3}He lung imaging, a nominal spatial resolution of 4 mm was obtained without visible blurring compared to a spoiled-GRE pulse sequence, while the SNR for the TrueFISP sequence was 2-3 times that for the spoiled-GRE method [59,60].

Although diffusion-induced signal attenuation is reduced for TrueFISP compared to RARE, it can nonetheless be significant for TrueFISP as illustrated in Figure 3b for a flip angle of 180º. Because of this additional signal-loss mechanism, the flip angle that yields maximum signal for a TrueFISP pulse sequence with sequential phase encoding is substantially less for ^{3}He and ^{129}Xe gases than the value of 180º appropriate for hyperpolarized ^{13}C compounds. The decrease in the net transverse magnetization between successive RF pulses caused by diffusion is equivalent to that which would be caused by a reduction in the T2 [60,61], and we can thus estimate the effects of diffusion by calculating the corresponding effective T2 relaxation time. The relationship between T2 and maximum signal for a TrueFISP pulse sequence and a very long T1 relaxation time is illustrated in Figure 4. By reducing the flip angle below 180º, the fraction of the magnetization that is consumed each repetition is decreased, permitting the available magnetization to be distributed more evenly across the desired number of phase-encoding steps. (Note that

this will decrease the rate of signal decline below that shown in Figure 3b for a flip angle of 180º.) For example, for the readout-gradient *b* value of 0.046 s/cm^2 reported in reference 54, diffusion attenuation results in an effective T2 of approximately 109 ms for an ADC of 0.2 cm^2/s (value for ^{3}He in healthy lung tissue for a diffusion time of a few ms; it is assumed that the T2 of the gas is much longer than 109 ms) and thus Figure 4 indicates that a flip angle of 55º would provide maximum signal. Diffusion-induced signal attenuation from the phase-encoding and slice-select gradients can also be viewed as causing a reduction in the effective T2 relaxation time. For many cases of interest, the largest signal attenuation is from the readout gradient.

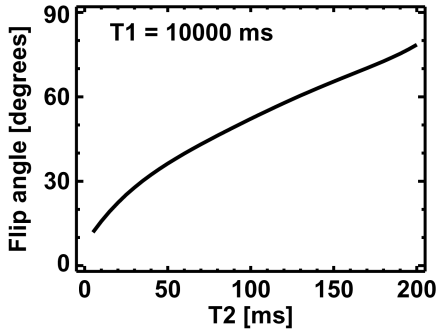

Figure 4. Flip angle for an ideal TrueFISP-type pulse sequence with a total acquisition time of 0.5 seconds (TR 4 ms, sequential phase encoding, 128 phase-encoding steps, half-angle preparation pulse [49], T1 10000 ms) that provides the maximum signal for a given T2 relaxation time. The signal is calculated as that associated with the central phase-encoding step.

Although the spatial resolution that can be obtained for hyperpolarized-gas lung imaging with a standard RARE pulse sequence is limited by diffusion-induced signal attenuation as discussed above, potential approaches to minimize the diffusion sensitivity for this class of pulse sequences to permit both high SNR and high spatial resolution (~3 mm) have been suggested [61,62].

Based on the discussion above, a TrueFISP-type pulse sequence may appear to be very appealing for hyperpolarized-gas imaging. However, susceptibility artifacts in the form of dark bands are seen near the diaphragmatic border with this technique at the commonly used field strength of 1.5 Tesla [59,60]. It may be possible to suppress these artifacts by imaging at lower field strengths, and at such field strengths TrueFISP may be the preferred technique for a number of hyperpolarized-gas applications. Nonetheless, all factors considered, low-flip-angle, spoiled GRE imaging is currently the most-widely used technique for ^{3}He and ^{129}Xe gases and thus it is worthwhile to comment on diffusion effects for conventional GRE as well.

For many parameter sets of practical interest, the readout gradient is the dominant source of diffusion-induced signal attenuation [63]. By assuming an idealized waveform for the readout gradient (ramp times equal to zero, equal gradient magnitudes for the prephasing and readout portions of the waveform, and symmetric sampling of the echo), a very simple expression for the *b* value at the echo time can be derived:

$$b = \frac{\pi^2 T_S}{3(\Delta x)^2}, \qquad [2]$$

where Δx is the nominal spatial resolution and T_S is the duration of the data-sampling period. The corresponding signal attenuations at the echo time are shown in Figure 5 for ^{3}He and ^{129}Xe ADC values associated with these gases in the healthy human lung and in air. For all cases considered, substantial signal loss is predicted for nominal spatial resolutions less than 1 mm. The signal attenuation at the echo time can be reduced by using asymmetric sampling of the echo [63], spiral sampling or radial sampling.

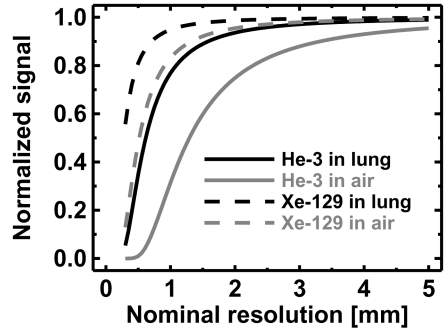

Figure 5. Diffusion-induced signal attenuation at the echo time versus nominal spatial resolution for ^{3}He and ^{129}Xe gases in the healthy human lung (ADC: 0.2 cm^2/s for ^{3}He and 0.04 cm^2/s for ^{129}Xe) or in air (ADC: 0.88 cm^2/s for ^{3}He and 0.14 cm^2/s for ^{129}Xe). Calculations were based on Equation [2] (an ideal GRE readout gradient waveform with ramp times equal to zero, equal gradient magnitudes for the prephasing and readout portions of the waveform, and symmetric sampling of the echo) and a data sampling period of 4 ms.

The principles regarding diffusion-induced signal attenuation that were discussed in this section apply equally to ^{3}He and ^{129}Xe, although ^{129}Xe has a substantially lower diffusion coefficient (Table 1), which results in a lower diffusion-induced signal loss for a given *b* value. However, in terms of signal loss during the echo train of pulse sequences such as TrueFISP or FSE/TSE, exchange of ^{129}Xe within the lung between gas and dissolved phases effectively shortens the T2 relaxation time [64], and thus offsets to some extent xenon's advantage of a lower diffusion coefficient.

Flip Angles and Phase-encoding Order for GRE Pulse Sequences

As noted above, a low-flip-angle, spoiled GRE pulse sequence is often used for hyperpolarized-gas applications. For this technique, the choices made for the flip angles and phase-encoding order play a critical role in the resulting image quality [63,65]. Given the non-equilibrium nature of the hyperpolarized magnetization, one obvious choice for the flip angles is the variable flip-angle series that distributes the magnetization uniformly across all phase-encoding steps and uses all of the available magnetization [66,67]. However, in practice, the desired flip angles might not be obtained due to miscalibration of the transmitter (standardized transmitter calibration procedures do not exist for hyperpolarized substances) or an inhomogeneous transmit field (B_1) for the RF coil [65]. Figure 6 illustrates how the signal evolutions for a spoiled GRE pulse sequence that uses either variable or constant flip angles are predicted to vary from the desired values when the chosen flip angles are not obtained [68]. During the initial part of the acquisition, a 20% variation in the flip angles results in deviations of the signals from their desired values that are similar for both variable and constant flip angles. However, during the latter part of the acquisition, a 20% variation in the flip angles results in signal deviations for variable flip angles that are much larger than those for constant flip angles. Thus, the point-spread function that corresponds to constant flip angles would be more stable against a 20% variation in the flip angles than that which corresponds to variable flip angles. In addition, if sequential phase encoding is used, the signal intensity at the center of *k* space for constant flip angles is fairly insensitive to moderate variations of the flip angle from its desired value [65]. A constant-flip-angle acquisition with sequential phase encoding has the disadvantage that the maximum signal (neglecting T1 relaxation) is 14% less than that for the ideal variable-flip-angle acquisition. Considering the B_1 variations typically encountered in practice, it is unlikely that this advantage of variable flip angles can currently be realized. Nonetheless, auto-calibrating methods are under investigation that would permit the desired uniform signal evolution to be obtained with variable flip angles regardless of the accuracy of the transmitter calibration [68,69].

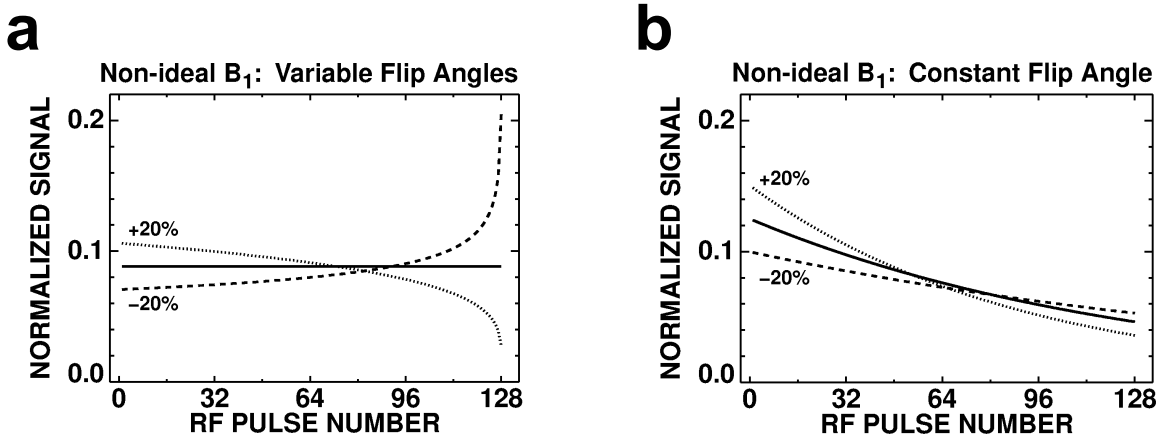

Figure 6. Theoretical calculations of signal versus RF pulse number for a spoiled GRE sequence (128 phase -encoding steps) that uses (**a**) variable or (**b**) constant flip-angle RF pulses. For both cases, the solid line denotes the signal evolution for the desired flip angles, and the dotted and dashed lines correspond to flip angles that are 20% higher than desired and 20% lower than desired, respectively. For (**a**), the desired flip angles are those that yield a uniform signal and use all of the magnetization. For (**b**), the desired flip angle is that which produces the maximum signal halfway through the acquisition (pulse number 64). Slice-profile, diffusion and T1-relaxation effects were not included in the calculations. The effects of spatial variations in the reception sensitivity of the RF coil [65] were also not included in the calculations.

Given that a constant-flip-angle acquisition appears to be a good choice considering practical constraints, we next need to choose the value for the constant flip angle and the phase-encoding order. As illustrated in Figure 6b, the application of constant-flip-angle RF pulses results in a gradually declining signal as the non-equilibrium magnetization is depleted during the acquisition. The flip angle should be chosen considering the form of the resulting *k*-space filter and the signal intensity that is obtained for the central portion of *k* space – both of which depend on the phase-encoding order. Figure 7 illustrates the interplay between signal and resolution (calculated as the full-width at half maximum of the associated point spread function, which is the Fourier transform of the *k*-space filter) for centric and sequential phase-encoding orders. It is easy to show [70] that the peak signal for sequential phase encoding occurs for the flip angle:

$$\theta = \operatorname{atan}\frac{1}{\sqrt{n_o - 1}}, \qquad [3]$$

where n_o is the phase-encoding step corresponding to the center of *k* space. For the number of phase-encoding steps considered in Figure 7 this flip angle is approximately 7º, which corresponds to a normalized resolution of 0.96 (i.e., a very slight blurring). For centric phase encoding, this same resolution corresponds to a signal intensity that is about 20% less than that for sequential phase encoding. Thus, if our goal is to minimize blurring, a good choice is sequential phase encoding with the flip angle provided by Equation [3]. On the other hand, if some blurring can be tolerated, higher signal intensities can be obtained with centric phase encoding [63]. For example, for a normalized resolution of 0.8, the signal intensity for centric phase encoding is roughly double the maximum signal intensity that can be obtained with sequential phase encoding. A partial-Fourier acquisition can be used with centric phase encoding to reduce the blurring associated with a given flip angle [63].

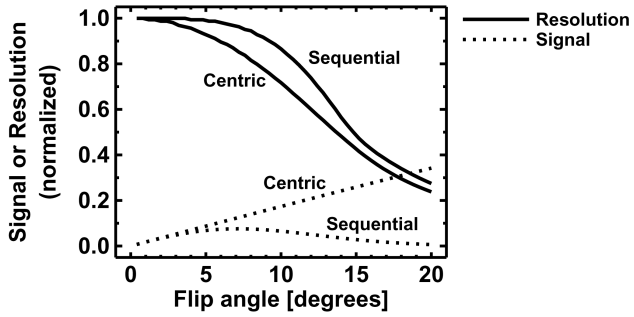

Figure 7. Theoretical calculations of signal (dotted lines) and resolution (solid lines) versus flip angle for a spoiled GRE sequence (128 phase-encoding steps) that uses sequential or centric phase encoding. Resolution was calculated as the reciprocal of the full-width at half maximum of the associated point spread function, normalized by that corresponding to a uniform signal evolution. Slice-profile, diffusion and T1-relaxation effects were not included in the calculations.

There are other important factors that were not included in our discussion above, but should be kept in mind. Although T1 relaxation times for hyperpolarized substances are typically very long, T1-induced signal decay can become relevant for very long measurements such as 3D acquisitions of the whole lung [71]. Due to the non-equilibrium nature of the magnetization, the profile for slice-selective pulses varies in shape throughout the acquisition [63,65]. This behavior modifies the signal evolution compared to that obtained for an ideal slice profile [63,65], and also causes the signal evolution to depend strongly on the gap between slices [65]. Nonetheless, the behaviors of the signal evolutions corresponding to ideal and actual slice profiles are often qualitatively similar.

Closing Remarks

Certain characteristics of hyperpolarized nuclei differ substantially from those for water or lipid protons in biological tissues and thus these differences play an important role in the selection and optimization of appropriate pulse sequences for imaging of hyperpolarized substances. For some techniques and applications, the parameter values suitable for imaging of hyperpolarized substances are quite different than those that are typically used for proton imaging, while for others, pulse sequences that are commonly used for proton imaging are not suitable for use with hyperpolarized substances.

References

1. Middleton H, Black RD, Saam B, et al. MR imaging with hyperpolarized ^{3}He gas. Magn Reson Med 1995; 33:271-275.
2. Black RD, Middleton HL, Cates GD, et al. In vivo He-3 MR images of guinea pig lungs. Radiology 1996; 199:867-870.

3. MacFall JR, Charles HC, Black RD, et al. Human lung air spaces: potential for MR imaging with hyperpolarized He-3. Radiology 1996; 200:553-558.
4. Kauczor HU, Hofmann D, Kreitner KF, et al. Normal and abnormal pulmonary ventilation: visualization at hyperpolarized He-3 MR imaging. Radiology 1996; 201:564-568.
5. Albert MS, Cates GD, Driehuys B, et al. Biological magnetic resonance imaging using laser-polarized ^{129}Xe. Nature 1994; 370:199-201.
6. Wagshul ME, Button TM, Li HF, et al. In vivo MR imaging and spectroscopy using hyperpolarized ^{129}Xe. Magn Reson Med 1996; 36:183-191.
7. Swanson SD, Rosen MS, Agranoff BW, et al. Brain MRI with laser-polarized ^{129}Xe. Magn Reson Med 1997; 38:695-698.
8. Mugler JP III, Driehuys B, Brookeman JR, et al. MR imaging and spectroscopy using hyperpolarized ^{129}Xe gas: Preliminary human results. Magn Reson Med 1997; 37:809-815.
9. Golman K, Axelsson O, Jóhannesson H, Månsson S, Olofsson C, Petersson JS. Parahydrogen-induced polarization in imaging: Subsecond ^{13}C angiography. Magn Reson Med 2001; 46:1–5.
10. Golman K, Ardenkjær-Larsen JH, Petersson JS, Månsson S, Leunbach I. Molecular imaging with endogenous substances. Proc Natl Acad Sci USA 2003; 100:10435–10439.
11. Johansson E, Månsson S, Wirestam R, et al. Cerebral perfusion assessment by bolus tracking using hyperpolarized ^{13}C. Magn Reson Med 2004; 51:464–472.
12. Johansson E, Olsson LE, Månsson S, et al. Perfusion assessment with bolus differentiation: A technique applicable to hyperpolarized tracers. Magn Reson Med 2004; 52:1043–1051.
13. Bock M. Simultaneous T_2* and diffusion measurements with ^{3}He. Magn Reson Med 1997; 38:890-895.
14. Patyal BR, Gao JH, Williams RF, et al. Longitudinal relaxation and diffusion measurements using magnetic resonance signals from laser-hyperpolarized ^{129}Xe nuclei. J Magn Reson 1997; 126:58-65.
15. Abraham MH, Kamlet MJ, Taft RW, Doherty RM, Weathersby PK. Solubility properties in polymers and biological media. 2. The correlation and prediction of the solubilities of non-electrolytes in biological tissues and fluids. J Med Chemistry 1985; 28:865-870.
16. Kastler A. J Phys Rad 1950; 11:255-265.
17. Bouchiat MA, Carver TR, Varnum CM. Nuclear polarization in ^{3}He gas induced by optical pumping and dipolar exchange. Phys Rev Lett 1960; 5:373-375.
18. Colegrove FD, Schearer LD, Walters GK. Polarization of He^3 gas by optical pumping. Phys Rev 1963; 132:2561-2572.
19. Surkau R, Becker J, Ebert M, et al. Realization of a broad band neutron spin filter with com-pressed, polarized ^{3}He gas. Nucl Instr Meth A 1997; 444-450.
20. Bowers CR, Weitekamp DP. Parahydrogen and synthesis allow dramatically enhanced nuclear alignment. J Am Chem Soc 1987; 109:5541-5542.
21. Natterer J, Bargon J. Parahydrogen induced polarization. Progr Nucl Magn Reson Spectrosc 1997; 31:293-315.
22. de Boer W, Borghini M, Morimoto K, Niinikoski TO, Udo F. Dynamic polarization of protons, deuterons, and carbon-13 nuclei: thermal contact between nuclear spins and an electron spin-spin interaction reservoir. J Low Temp Phys 1974; 15:249-267.
23. Hall DA, Maus DC, Gerfen GJ, et al. Polarization-enhanced NMR spectroscopy of biomolecules in frozen solution. Science 1997; 276:930-932.
24. Song YQ, Gaede HC, Pietrass T, et al. Spin-polarized ^{129}Xe gas imaging of materials. J Magn Reson 1995; A115:127-130.
25. Hagspiel KD, Altes TA, Mugler JP III, et al. MR virtual colonography using hyperpolarized ^{3}He as an endoluminal contrast agent: Demonstration of feasibility. Magn Reson Med 2000; 44:813-816.
26. Rizi RR, Dimitrov IE, Thompson A, et al. MRI of hyperpolarized ^{3}He gas in human paranasal sinuses. Magn Reson Med 1998; 39:865-868.
27. Edelstein WA, Glover GH, Hardy CJ, Redington RW. The intrinsic signal-to-noise ratio in NMR imaging. Magn Reson Med 1986; 3:604-618.

28. Chen XJ, Hedlund LW, Möller HE, Chawla MS, Maronpot RR, Johnson GA. Detection of emphysema in rat lungs by using magnetic resonance measurements of ^{3}He diffusion. Proc Natl Acad Sci USA 2000; 97:11478-11481.
29. Saam BT, Yablonskiy DA, Kodibagkar VD, et al. MR imaging of diffusion of ^{3}He gas in healthy and diseased lungs. Magn Reson Med 2000; 44:174-179.
30. Salerno M, de Lange EE, Altes TA, Truwit JD, Brookeman JR, Mugler JP III. Emphysema: Hyperpolarized helium 3 diffusion MR imaging of the lungs compared with spirometric indexes -- Initial experience. Radiology 2002; 222:252-260.
31. Miller KW, Reo NV, Uiterkamp AJMS, Stengle DP, Stengle TR, Williamson KL. Xenon NMR: chemical shifts of a general anesthetic in common solvents, proteins, and membranes. Proc Natl Acad Sci USA 1981; 78:4946-4949.
32. Bifone A, Song YQ, Seydoux R, et al. NMR of laser-polarized xenon in human blood. Proc Natl Acad Sci USA 1996; 93:12932-12936.
33. Goodson BM, Song Y, Taylor RE, et al. In vivo NMR and MRI using injection delivery of laser-polarized xenon. Proc Natl Acad Sci USA 1997; 94:14725-14729.
34. Chawla MS, Chen XJ, Möller HE, et al. In vivo MR vascular imaging using laser-polarized ^{3}He microbubbles. Proc Natl Acad Sci USA 1998; 95:10832-10835.
35. Svensson J, Månsson S, Johansson E, Petersson JS, Olsson LE. Hyperpolarized ^{13}C MR angiography using TrueFISP. Magn Reson Med 2003; 50:256–262.
36. Sakai K, Bilek AM, Oteiza E, et al. Temporal dynamics of hyperpolarized ^{129}Xe resonance in living rats. J Magn Reson 1996; 111:300-304.
37. Ruppert K, Brookeman JR, Hagspiel KD, Driehuys B, Mugler JP III. NMR of hyperpolarized ^{129}Xe in the canine chest: Spectral dynamics during a breath-hold. NMR Biomed 2000; 13:220-228.
38. Ruppert K, Brookeman JR, Hagspiel KD, Mugler JP III. Probing lung physiology with xenon polarization transfer contrast (XTC). Magn Reson Med 2000; 44:349-357.
39. Butler JP, Mair RW, Hoffmann D, et al. Measuring surface-area-to-volume ratios in soft porous materials using laser-polarized xenon interphase exchange nuclear magnetic resonance. J Phys: Condens Matter 2002; 14:L297–L304.
40. Ruppert K, Mata JF, Brookeman JR, Hagspiel KD, Mugler JP III. Exploring lung function with hyperpolarized ^{129}Xe nuclear magnetic resonance. Magn Reson Med 2004; 51:676-687.
41. Deninger AJ, Eberle B, Ebert M, et al. Quantification of regional intrapulmonary oxygen partial pressure evolution during apnea by ^{3}He MRI. J Magn Reson 1999; 141:207-216.
42. Deninger AJ, Eberle B, Bermuth J, et al. Assessment of a single-acquisition imaging sequence for oxygen-sensitive ^{3}He-MRI. Magn Reson Med 2002; 47:105-114.
43. Fischer MC, Spector ZZ, Ishii M, et al. Single-acquisition sequence for the measurement of oxygen partial pressure by hyperpolarized gas MRI. Magn Reson Med 2004; 52:766–773.
44. Wild JM, Fichele S, Woodhouse N, Paley MNJ, Kasuboski L, van Beek EJR. 3D volume-localized pO_2 measurement in the human lung with ^{3}He MRI. Magn Reson Med 2005; 53:1055–1064.
45. Goodson BM. Nuclear magnetic resonance of laser-polarized noble gases in molecules, materials, and organisms. J Magn Reson 2002; 155:157–216.
46. Oppelt A, Graumann R, Barfuss H, Fischer H, Hartl W, Schajor W. FISP - a new fast MRI sequence. Electromedica 1986; 54:15-18.
47. Becker ED, Ferretti JA, Farrar TC. Driven equilibrium fourier transform spectroscopy. A new method for nuclear magnetic resonance signal enhancement. J Am Chem Soc 1969; 91:7784-7785.
48. Scheffler K, Heid O, Hennig J. Magnetization preparation during the steady state: Fat-saturated 3D TrueFISP. Magn Reson Med 2001; 45:1075–1080.
49. Deimling M, Heid O. Magnetization prepared True FISP imaging. In: Proc Soc Magn Reson, 2nd Meeting, 1994; 495.
50. Yablonskiy DA, Sukstanskii AL, Leawoods JC, et al. Quantitative in vivo assessment of lung microstructure at the alveolar level with hyperpolarized ^{3}He diffusion MRI. Proc Natl Acad Sci USA 2002; 99:3111-3116.

51. Maier T, Knight-Scott J, Mai VM, Mugler JP III, Brookeman JR. Restricted diffusion of hyperpolarized ^{3}He in the human lung. In: Proc Intl Soc Magn Reson Med, 6th Meeting, 1998; 1913.
52. Salerno M, Brookeman JR, Mugler JP III. Time-dependent hyperpolarized ^{3}He diffusion MR imaging: Initial experience in healthy and emphysematous lungs. In: Proc Intl Soc Magn Reson Med, 9th Meeting, 2001; 950.
53. Fichele S, Paley MNJ, Woodhouse N, Griffiths PD, van Beek EJR, Wild JM. Investigating ^{3}He diffusion NMR in the lungs using finite difference simulations and in vivo PGSE experiments. J Magn Reson 2004; 167:1-11.
54. Woods JC, Yablonskiy DA, Chino K, Tanoli TS, Cooper JD, Conradi MS. Magnetization tagging decay to measure long-range ^{3}He diffusion in healthy and emphysematous canine lungs. Magn Reson Med 2004; 51:1002-1008.
55. Schreiber WG, Morbach AE, Stavngaard T, et al. Assessment of lung microstructure with magnetic resonance imaging of hyperpolarized Helium-3. Respir Physiol Neurobiol 2005; 148:23–42.
56. Turner R, Le Bihan D, Maier J, Vavrek R, Hedges LK, Pekar J. Echo-planar imaging of intravoxel incoherent motion. Radiology 1990; 177:407-414.
57. Hennig J, Nauerth A, Friedburg H. RARE imaging: A fast imaging method for clinical MR. Magn Reson Med 1986; 3:823-833.
58. Durand E, Guillot G, Darrasse L, et al. CPMG measurements and ultrafast imaging in human lungs with hyperpolarized helium-3 at low field (0.1 T). Magn Reson Med 2002; 47:75-81.
59. Mugler JP III, Salerno M, de Lange EE, Brookeman JR. Optimized TrueFISP hyperpolarized ^{3}He MRI of the lung yields a 3-fold SNR increase compared to FLASH. In: Proc Intl Soc Magn Reson Med, 10th Meeting, 2002; 2019.
60. Wild JM, Kasuboski L, Teh K, Woodhouse N, Fichele S, Paley MN. SSFP imaging with hyperpolarized 3He: Experiments and simulations. In: Proc Intl Soc Magn Reson Med, 13th Meeting, 2005; 50.
61. Mugler JP III, Salerno M, Brookeman JR. Reducing diffusion-induced signal loss in hyperpolarized ^{3}He MRI. In: Proc Intl Soc Magn Reson Med, 10th Meeting, 2002; 2018.
62. Mugler JP III, Ruppert K, Tobias WA, Cates GD Jr., de Lange EE, Brookeman JR. Circular-trajectory RARE imaging for increased SNR in ^{3}He lung MRI. In: Proc Intl Soc Magn Reson Med, 13th Meeting, 2005; 1817.
63. Wild JM, Paley MN, Viallon M, Schreiber WG, van Beek EJ, Griffiths PD. *k*-space filtering in 2D gradient-echo breath-hold hyperpolarized ^{3}He MRI: Spatial resolution and signal-to-noise ratio considerations. Magn Reson Med 2002; 47:687-695.
64. Ruppert K, Mata J, Brookeman J, et al. ^{129}Xe lung imaging with a single-shot circular RARE sequence. In: Proc Intl Soc Magn Reson Med, 12th Meeting, 2004; 1687.
65. Miller GW, Altes TA, Brookeman JR, de Lange EE, Mugler JP III. Hyperpolarized ^{3}He lung ventilation imaging with B_1-inhomogeneity correction in a single breath-hold scan. MAGMA 2004; 16:218-226.
66. Mansfield P. Spatial mapping of the chemical shift in NMR. Magn Reson Med 1984; 1:370-386.
67. Zhao L, Mulkern R, Tseng CH, et al. Gradient-echo imaging considerations for hyperpolarized ^{129}Xe MR. J Magn Reson, Series B 1996; 113:179-183.
68. Miller GW, Altes TA, Brookeman JR, Mata JF, de Lange EE, Mugler JP III. Getting the most from a dose: Feedback-optimized signal rationing in 3D hyperpolarized gas MRI. 2004 International Workshop on Pulmonary Functional Imaging at Penn, Philadelphia.
69. Miller GW, Altes TA, Brookeman JR, de Lange EE, Mata JF, Mugler JP III. Improving the quality of 3D hyperpolarized gas images using feedback-controlled flip-angle evolution. In: Proc Intl Soc Magn Reson Med, 12th Meeting, 2004; 1681.
70. Mugler JP III. Optimization of gradient-echo sequences for hyperpolarized noble gas MRI. In: Proc Intl Soc Magn Reson Med, 6th Meeting, 1998; 1904.
71. Wild JM, Woodhouse N, Paley MNJ, et al. Comparison between 2D and 3D gradient-echo sequences for MRI of human lung ventilation with hyperpolarized ^{3}He. Magn Reson Med 2004; 52:673–678.